Spiral chain O_4 form of dense oxygen

Li Zhu[a,1], Ziwei Wang[a,1], Yanchao Wang[a], Guangtian Zou[a], Ho-kwang Mao[b,2], and Yanming Ma[a,c,2]

[a]State Key Laboratory of Superhard Materials, Jilin University, Changchun 130012, China; [b]Geophysical Laboratory, Carnegie Institution of Washington, Washington, DC 20015; and [c]Beijing Computational Science Research Center, Beijing 100084, China

Contributed by Ho-Kwang Mao, November 29, 2011 (sent for review November 1, 2011)

Oxygen is in many ways a unique element: It is the only known diatomic molecular magnet, and it exhibits an unusual O_8 cluster in its high-pressure solid phase. Pressure-induced molecular dissociation as one of the fundamental problems in physical sciences has been reported from theoretical or experimental studies of diatomic solids H_2, N_2, F_2, Cl_2, Br_2, and I_2 but remains elusive for molecular oxygen. We report here the prediction of the dissociation of molecular oxygen into a polymeric spiral chain O_4 structure (space group $I4_1/acd$, θ-O_4) above 1.92-TPa pressure using the particle-swarm search method. The θ-O_4 phase has a similar structure as the high-pressure phase III of sulfur. The molecular bonding in the insulating ε-O_8 phase or the isostructural superconducting ζ-O_8 phase remains remarkably stable over a large pressure range of 0.008–1.92 TPa. The pressure-induced softening of a transverse acoustic phonon mode at the zone boundary V point of O_8 phase might be the ultimate driving force for the formation of θ-O_4. Stabilization of θ-O_4 turns oxygen from a superconductor into an insulator by opening a wide band gap (approximately 5.9 eV) that originates from the sp^3-like hybridized orbitals of oxygen and the localization of valence electrons.

solid oxygen | spiral chain structure

As a long-standing problem in physics and chemistry, as well as earth and planetary sciences, high-pressure dissociation of diatomic molecules, such as H_2, N_2, O_2, F_2, Cl_2, Br_2, and I_2, has attracted a lot of attention. Among these molecular systems, solid oxygen is a system of particular interest and exhibits many unusual physical properties by virtue of its molecular spin and the resultant spin-spin interactions, which make the system a critical test case for condensed-matter theory (1, 2). Oxygen is also the third most abundant element in the Solar System, and its behavior under extreme pressures provides important insight into the oxygen-related systems for a better understanding of the physics and chemistry of planetary interiors.

Oxygen exhibits a rich polymorphism with seven unambiguously established crystalline phases. Upon cooling at ambient pressure, oxygen is in turn solidified to the paramagnetic γ-phase, the magnetically disordered (short-range ordered) β-phase (3, 4), and ultimately the antiferromagnetic α-phase (5). Upon compressing to approximately 6 GPa, the α-phase transforms into the antiferromagnetic δ-phase (6–8). Under a higher pressure of approximately 8 GPa, the magnetic order of oxygen is destroyed, which leads to the ε-O_8 phase consisting of O_8 clusters (9, 10). The ε-O_8 phase displays the bonding characteristics of a closed-shell system, in which the intermolecular interactions primarily involve the half-filled $1\pi_g{}^*$ orbital of O_2 (11). Above 96 GPa, ε-O_8 has been observed to transform into a metallic ζ-phase (12, 13) and intriguingly exhibits superconductivity with a transition temperature of 0.6 K (14). This superconducting ζ-phase has been predicted by theory (15) and subsequently confirmed by experiment (16) to be isostructural with ε-O_8, except that the ζ-O_8 phase has a shorter O-O distance between O_8 clusters than between O_2 pairs within an O_8 cluster. These studies have explored the high-pressure phase diagrams of solid oxygen up to the maximum pressure of 500 GPa (15). At such pressures, other diatomic molecules (17–21) readily exhibit molecular dissociations, whereas the O_2 molecules remain intact.

In this work, we have extensively explored the high-pressure crystal structures of solid oxygen up to 2 TPa by using the first-principles method of crystal structure prediction (22), which was designed to perform global minimization of free energy surfaces. This analysis was conducted by merging ab initio total-energy calculations via the CALYPSO (crystal structure analysis by particle-swarm optimization) method (22). Our CALYPSO method has been implemented in the CALYPSO code and successfully benchmarked on a number of known systems (22). Several predictions of high-pressure structures of dense Li, Mg, Bi_2Te_3, and water ice (23–26) were successfully made, and predictions of the high-pressure insulating *Aba*2-40 (Pearson symbol oC40) structure of Li and the two low-pressure monoclinic structures of Bi_2Te_3 were confirmed by independent experiments (25, 27).

Results and Discussion

Our structure searches using the CALYPSO code with system sizes that were up to 24 atoms per simulation cell were performed at pressures of 0.02–2 TPa. The structural simulations at 0.02 TPa were able to successfully predict the experimentally observed ε-O_8 structure, whereas at 0.1–1.5 TPa, ζ-O_8 was predicted to be stable, which is in agreement with an earlier prediction (15) and experimental observation (16). At 2 TPa, we surprisingly discovered an energetically most stable tetragonal $I4_1/acd$ structure (named θ-O_4, 16 atoms per cell, Fig. 1*A*), which is slightly denser (approximately 1.3%) than ζ-O_8. Remarkably, the molecular feature is no longer preserved in the θ-O_4 structure; instead, squared chains with four atoms per turn are formed. In this configuration, each oxygen atom has two identical nearest neighbors with a nearest O-O distance of 1.153 Å at 2 TPa, which is considerably larger than the intramolecular distances (e.g., 1.036 Å at 1.8 TPa) in ζ-O_8. The chains are formed along the c axis with an O-O-O bond angle of 98.79°. The nearest-neighbor O-O distance between chains is 1.552 Å, which is approximately 35% longer than the intrachain O-O distance. Calculating the enthalpy curve (Fig. 2*A*) at a higher level of accuracy for θ-O_4 confirms its energetic stability relative to ζ-O_8. Phonon calculations (*SI Text*) establish the dynamical stability of the θ-O_4 structure because we do not find any imaginary phonon within the Brillouin zone.

Oxygen is the lightest element in group VI of the periodic table, with sulfur being the next heavier family member. Previous theoretical studies assumed that the molecular ring structure of S_8 (S-I) in sulfur might be one of the candidates for the high-pressure phases of solid oxygen (28). However, calculations suggested that oxygen in the S_8 structure was energetically very unfavorable when compared with other known oxygen phases. Interestingly, we found that θ-O_4 shares the same structure type as the high-pressure S_4 phase (S-III) of sulfur (29). The reasons why atomic oxygen is unable to adopt the lower pressure phases (S-I and the

---

Author contributions: Y.M. designed research; L.Z., Z.W., Y.W., and Y.M. performed research; L.Z., Z.W., Y.W., G.Z., H.-K.M., and Y.M. analyzed data; and L.Z., Z.W., G.Z., H.-K.M., and Y.M. wrote the paper.

The authors declare no conflict of interest.

[1] L.Z. and Z.W. contributed equally to this work.

[2] To whom correspondence may be addressed. E-mail: mym@jlu.edu.cn or h.mao@gl.ciw.edu.

This article contains supporting information online at www.pnas.org/lookup/suppl/doi:10.1073/pnas.1119375109/-/DCSupplemental.

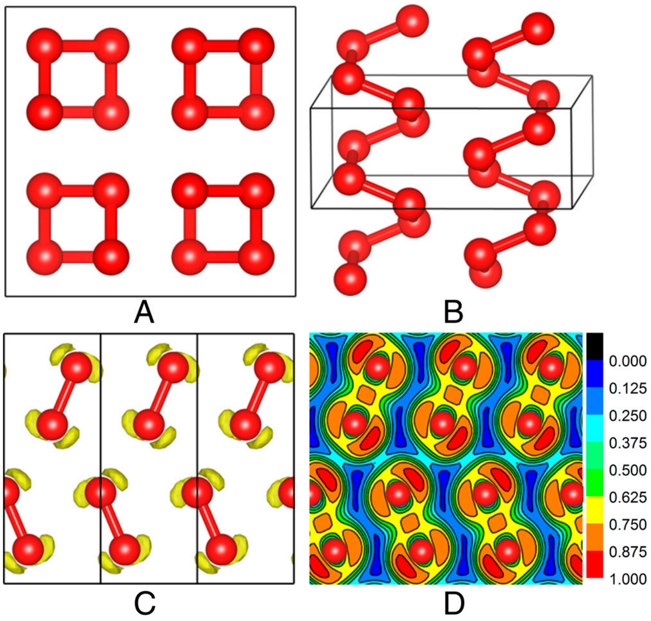

Fig. 1. (*A* and *B*) The predicted θ-O_4 structure viewed along the *c* and *a* axes, respectively. The optimized lattice parameters at 2 TPa are $a = 5.651$ Å and $c = 1.803$ Å with oxygen occupying 16*f* (0.1359, 0.3859, 0.125) positions. (*C*) The calculated ELF isosurface of the θ-O_4 structure with ELF = 0.8. (*D*) ELF plots in the (100) section.

trigonal chain S-II) of sulfur might stem from the fact that oxygen has a very small 1*s* core (the 1*s* orbital radius of oxygen is 0.068 Å) which is capable of forming very short bonds. This small 1*s* core in oxygen is apparently in contrast to the much larger 2*p* core in sulfur (the 2*p* orbital radius of sulfur is 0.169 Å).

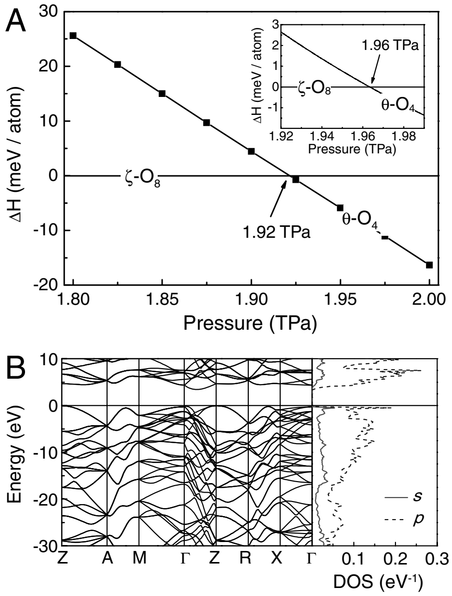

Fig. 2. (*A*) Calculated enthalpy per atom as a function of pressure with respect to ζ-O_8. For confirmation, the *Inset* in *A* shows the enthalpy of θ-O_4 relative to that of ζ-O_8 that was obtained by a full-potential all-electron calculation using WIEN2K code. The all-electron method finds basically the same result on the transition pressure with a <2% difference, which confirms the validity of the PAW potential adopted here at such high pressures. *B* shows the band structure (*Left*) and partial electronic density of states (DOS, *Right*) for θ-O_4 at 2 TPa.

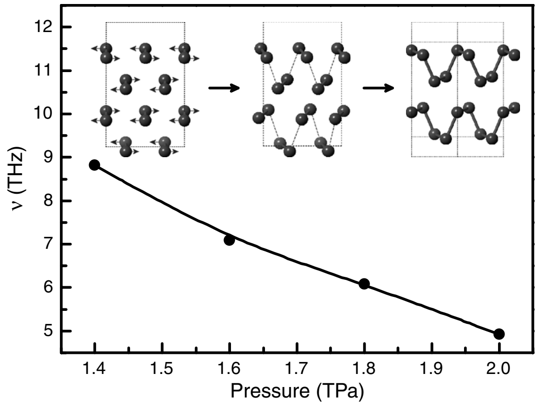

Fig. 3. Phonon frequencies of the softened transverse acoustic phonon mode at the zone boundary *V* point versus pressure in ζ-O_8. The *Inset* shows the phase transition mechanism of ζ-$O_8 \rightarrow \theta$-O_4. Arrows indicate the eigenvector of this softened mode.

To understand the driving force for the formation of polymeric θ-O_4 structure, we calculated the phonon dispersion curves of ζ-O_8 at elevated pressures. A transverse acoustic (TA) phonon mode at the zone boundary *V* point was found to soften linearly with increasing pressure (Fig. 3). It is well established that imaginary phonons (i.e., phonon frequencies having negative values) lead to the lattice instability and thus induce phase transitions (30, 31). Notably, even though at the phase transition pressure of 1.92 TPa the TA(*V*) phonon frequency in ζ-O_8 does not soften to zero or become imaginary, it can still initiate the phase transition. This transition mechanism is similar to those observed in SiO_2 (32) and MgH_2 (33), where the rutile → $CaCl_2$ phase transition is driven by the softened nonzero optical mode at the zone center (33). We have plotted the eigenvectors of this TA(*V*) phonon mode (Fig. 3, *Inset*), where the arrows represent the directions of atomic vibrations. It is clearly seen that this softening phonon mode is involved in the planar rotation of oxygen molecules around the *a* axis. The role of this rotation is to effectively shorten the intermolecular O-O distance and lengthen the intramolecular bond, which ultimately leads to the stabilization of the squared chains in the θ-O_4.

The metallization of ζ-O_8 is attributed to the creation of nearly free electrons by the pressure-induced band overlap (15). As a result, a very low electronic density of states is achieved at the Fermi level in close correlation with the observed low superconducting transition temperature (0.6 K) (14). As the atomic θ-O_4 phase forms, solid oxygen remarkably turns to an insulator as suggested by the simulated band structure and partial electronic density of states at 2 TPa (Fig. 2*B*). The calculated band gap is approximately 3.2 eV, although it should be much larger because the density functional calculation is known to significantly underestimate the band gap. A Heyd-Scuseria-Ernzerhof (HSE) hybrid function was adopted to correct the underestimation problem and to derive a better band gap estimation of approximately 5.9 eV. To probe the physical mechanism of this insulation, we have performed a chemical bonding analysis of θ-O_4 through calculations of the electron localization function (ELF) as shown in Fig. 1 *C* and *D*. In these figures, the calculated ELF isosurface clearly indicates two lone pairs and two O-O covalent bondings for each oxygen atom. This result allows us to identify the peculiar sp^3-like bonding orbitals of oxygen in θ-O_4. Consequently, a full localization of valence electrons is found, and this system creates a wide gap insulator. The intriguing bonding behavior of oxygen in θ-O_4 is not completely unexpected because it somewhat resembles the chemistry of oxygen in water ice, which forms two O-H single bonds. What makes it unique, however, is that the sp^3 orbitals of oxygen in θ-O_4 are distributed along infinite chains, unlike the perfect localization in isolated water molecules. Notably, the O-O-O bond angle is 98.79° in θ-O_4, which is evidently smaller than the ideal tetrahedral angle of 109°. This angle deviation is a result of Coulomb repulsive interaction between the lone pairs.

The insulating feature in θ-O_4 stands in contrast to the metallicity of the high-pressure atomic phases predicted for hydrogen (17) and established for halogens (18, 19). This contrast originates from the fact that hydrogen and halogen elements, having one and seven electrons in their outer shells, respectively, are unable to form the perfect saturation bonding in atomic structures favorable to the metallicity. This insulation in θ-O_4 seemingly resembles polymeric nitrogen (21, 34) in which five valence electrons of each N atom form three covalent bonds and one lone pair, which results in the complete localization of the valence electrons. However, creation of the insulating θ-O_4 from the compression of a metallic (and superconducting) solid clearly goes against the conventional wisdom that high pressure metallizes materials. The predicted formation of θ-O_4 in dense oxygen provided another case on the metal-insulator transition as previously exemplified in dense lithium (24, 35) and sodium (36) and represents a significant step forward in understanding the behavior of solid oxygen and other oxygen-related materials at extreme conditions, such as in the interiors of giant planets.

Methods

The underlying ab initio structural relaxations and electronic calculations were performed in the framework of density functional theory within the Perdew-Burke-Ernzerhof (PBE) theory, as implemented in the Vienna Ab Initio Simulation Package code (37). We also applied the HSE hybrid functions (38, 39) to correct the band gap error of the PBE functional. The all-electron projector augmented wave (PAW) (40, 41) method was adopted, with the PAW potential treating $1s^2$ as the core. The cutoff energy (910 eV) for the expansion of the wave function into plane waves and Monkhorst-Pack k (42) meshes were chosen to ensure that all of the enthalpy calculations are well converged to better than 1 meV per atom. The phonon calculations were carried out by using a supercell approach (43) as implemented in the phonopy code (44). The validity of the used PAW potential for the currently studied high-pressure (≤ 2 TPa) scenarios was carefully verified by comparing it with the full-potential all-electron calculation using the WIEN2K code (45). In the full-potential calculations, the muffin-tin radii were chosen to be 0.97 a.u. for O. The plane-wave cutoff was defined as $K_{\max}R_{\mathrm{MT}} = 7$, where R_{MT} represents the muffin-tin radius and $K_{\max}$ denotes the maximum size of the reciprocal-lattice vectors. Convergence tests resulted in the choices of 1,000 k points for both the ζ-O_8 and the θ-O_4 phases in the electronic integration of the Brillouin zone.

ACKNOWLEDGMENTS. The authors acknowledge the High Performance Computing Center of Jilin University for supercomputer time and for funding from the National Natural Science Foundation of China under Grants 11025418 and 91022029, and the China 973 Program under Grant 2011CB808200. H.M. was supported by the EFree grant, which is an Energy Frontier Research Center funded by the US Department of Energy, Office of Science, Office of Basic Energy Sciences under Award DE-SC0001057.

1. Freiman YA, Jodl HJ (2004) Solid oxygen. *Phys Rep* 401:1–228.
2. Young DA (1991) *Phase Diagrams of the Elements* (University of California Press, Berkeley).
3. Horl E (1962) Structure and structure imperfections of solid β-oxygen. *Acta Crystallogr* 15:845–850.
4. LeSar R, Etters RD (1988) Character of the α—β phase transition in solid oxygen. *Phys Rev B* 37:5364–5370.
5. Meier RJ, Helmholdt RB (1984) Neutron-diffraction study of α- and β-oxygen. *Phys Rev B* 29:1387–1393.
6. Schiferl D, Cromer DT, Schwalbe LA, Mills RL (1983) Structure of "orange" $^{18}\mathrm{O}_2$ at 9.6 GPa and 297 K. *Acta Crystallogr B* 39:153–157.
7. Gorelli FA, Santoro M, Ulivi L, Hanfland M (2002) Crystal structure of solid oxygen at high pressure and low temperature. *Phys Rev B* 65:172106.
8. Goncharenko IN, Makarova OL, Ulivi L (2004) Direct determination of the magnetic structure of the delta phase of oxygen. *Phys Rev Lett* 93:055502.
9. Fujihisa H, et al. (2006) O_8 cluster structure of the epsilon phase of solid oxygen. *Phys Rev Lett* 97:085503.
10. Lundegaard LF, Weck G, McMahon MI, Desgreniers S, Loubeyre P (2006) Observation of an O_8 molecular lattice in the ε phase of solid oxygen. *Nature* 443:201–204.
11. Meng Y, et al. (2008) Inelastic x-ray scattering of dense solid oxygen: Evidence for intermolecular bonding. *Proc Natl Acad Sci USA* 105:11640–11644.
12. Desgreniers S, Vohra YK, Ruoff AL (1990) Optical response of very high density solid oxygen to 132 GPa. *J Phys Chem* 94:1117–1122.
13. Akahama Y, et al. (1995) New high-pressure structural transition of oxygen at 96 GPa associated with metallization in a molecular solid. *Phys Rev Lett* 74:4690–4693.
14. Shimizu K, Suhara K, Ikumo M, Eremets MI, Amaya K (1998) Superconductivity in oxygen. *Nature* 393:767–769.
15. Ma Y, Oganov AR, Glass CW (2007) Structure of the metallic zeta -phase of oxygen and isosymmetric nature of the ε-ζ phase transition: Ab initio simulations. *Phys Rev B* 76:064101.
16. Weck G, Desgreniers S, Loubeyre P, Mezouar M (2009) Single-crystal structural characterization of the metallic phase of oxygen. *Phys Rev Lett* 102:255503.
17. Pickard CJ, Needs RJ (2007) Structure of phase III of solid hydrogen. *Nat Phys* 3:473–476.
18. Fujii Y, et al. (1989) Evidence for molecular dissociation in bromine near 80 GPa. *Phys Rev Lett* 63:536–539.
19. Takemura K, Minomura S, Shimomura O, Fujii Y (1980) Observation of molecular dissociation of iodine at high pressure by x-ray diffraction. *Phys Rev Lett* 45:1881–1884.
20. Eremets MI, Hemley RJ, Mao H-k, Gregoryanz E (2001) Semiconducting non-molecular nitrogen up to 240 GPa and its low-pressure stability. *Nature* 411:170–174.
21. Ma Y, Oganov AR, Li Z, Xie Y, Kotakoski J (2009) Novel high pressure structures of polymeric nitrogen. *Phys Rev Lett* 102:065501.
22. Wang Y, Lv J, Zhu L, Ma Y (2010) Crystal structure prediction via particle-swarm optimization. *Phys Rev B* 82:094116.
23. Li P, Gao G, Wang Y, Ma Y (2010) Crystal structures and exotic behavior of magnesium under pressure. *J Phys Chem C* 114:21745–21749.
24. Lv J, Wang Y, Zhu L, Ma Y (2011) Predicted novel high-pressure phases of lithium. *Phys Rev Lett* 106:015503.
25. Zhu L, et al. (2011) Substitutional alloy of Bi and Te at high pressure. *Phys Rev Lett* 106:145501.
26. Wang Y, et al. (2011) High pressure partially ionic phase of water ice. *Nat Commun* 2:563.
27. Guillaume CL, et al. (2011) Cold melting and solid structures of dense lithium. *Nat Phys* 7:211–214.
28. Kim KS, Jang JH, Kim S, Mhin B-J, Schaefer HF (1990) Potential new high energy density materials: Cyclooctaoxygen O_8, including comparisons with the well-known cyclo-S_8 molecule. *J Chem Phys* 92:1887–1892.
29. Degtyareva O, et al. (2005) Novel chain structures in group VI elements. *Nat Mater* 4:152–155.
30. Li Y, et al. (2006) Phonon instabilities in rocksalt AgCl and AgBr under pressure studied within density functional theory. *Phys Rev B* 74:054102.
31. Xie Y, et al. (2007) Electronic and phonon instabilities in face-centered-cubic alkali metals under pressure studied using ab initio calculations. *Phys Rev B* 75:064102.
32. Choudhury N, Chaplot SL (2006) Ab initio studies of phonon softening and high-pressure phase transitions of α-quartz SiO_2. *Phys Rev B* 73:094304.
33. Zhang L, et al. (2007) CaCl_2-type high-pressure phase of magnesium hydride predicted by ab initio phonon calculations. *Phys Rev B* 75:144109.
34. Pickard CJ, Needs RJ (2009) High-pressure phases of nitrogen. *Phys Rev Lett* 102:125702.
35. Guillaume CL, et al. (2011) Cold melting and solid structures of dense lithium. *Nat Phys* 7:211–214.
36. Ma Y, et al. (2009) Transparent dense sodium. *Nature* 458:182–185.
37. Kresse G, Furthmüller J (1996) Efficient iterative schemes for ab initio total-energy calculations using a plane-wave basis set. *Phys Rev B* 54:11169–11186.
38. Heyd J, Scuseria GE, Ernzerhof M (2003) Hybrid functionals based on a screened Coulomb potential. *J Chem Phys* 118:8207–8215.
39. Paier J, et al. (2006) Screened hybrid density functionals applied to solids. *J Chem Phys* 124:154709.
40. Blochl PE (1994) Projector augmented-wave method. *Phys Rev B* 50:17953–17979.
41. Kresse G, Joubert D (1999) From ultrasoft pseudopotentials to the projector augmented-wave method. *Phys Rev B* 59:1758–1775.
42. Monkhorst HJ, Pack JD (1976) Special points for Brillouin-zone integrations. *Phys Rev B* 13:5188–5192.
43. Parlinski K, Li ZQ, Kawazoe Y (1997) First-principles determination of the soft mode in cubic ZrO_2. *Phys Rev Lett* 78:4063–4066.
44. Togo A, Oba F, Tanaka I (2008) First-principles calculations of the ferroelastic transition between rutile-type and CaCl_2 -type SiO_2 at high pressures. *Phys Rev B* 78:134106.
45. Blaha P, Schwarz K, Madsen GKH, Kvasnicka D, Luitz J (2001) *WIEN2K—An Augmented Plane Wave + Local Orbitals Program for Calculating Crystal Properties* (Technische Universität Wien, Wien, Austria).